Cluster counting studies in a SuperB drift chamber prototype

by

Samuel Rudy Dejong
B.Sc., Carleton University, 2009

A Thesis Submitted in Partial Fulfillment of the
Requirements for the Degree of

MASTER OF SCIENCE

in the Department of Physics and Astronomy

Cluster counting studies in a SuperB drift chamber prototype

by

Samuel Rudy Dejong
B.Sc., Carleton University, 2009

Supervisory Committee

Dr. John Michael Roney, Supervisor
(Department of Physics and Astronomy)

Dr. Robert Kowaleski, Departmental Member
(Department of Physics and Astronomy)

Supervisory Committee

Dr. John Michael Roney, Supervisor
(Department of Physics and Astronomy)

Dr. Robert Kowaleski, Departmental Member
(Department of Physics and Astronomy)

ABSTRACT

SuperB is a high luminosity e^+e^- collider experiment that is currently being designed to explore the flavour sector of particle physics. The detector at SuperB will contain a drift chamber, a gas filled device used to measure the momentum and identity of particles produced in the collisions. Particle identification in a drift chamber uses the measured amount of ionization deposited by the particle in the cells of the chamber, which provides a measurement of the particle speed. The ionization loss is traditionally measured by integrating the total charge released by the ionization after a gas amplification avalanche process. Since such a measurement has potentially large uncertainties associated with fluctuations in the gas amplification and other processes, it is possible that measuring the number of primary clusters of ionization caused by the particle could provide an improvement in the measurement of the ionization loss. The results of experiments performed at the University of Victoria and the TRIUMF laboratory M11 test beam using a SuperB drift chamber prototype to test the feasibility of counting clusters are presented here. The ability to separate muons and pions at the momenta explored in the TRIUMF testbeam was similar to the ability to separate pions and kaons at the higher momenta of SuperB. It was found that counting the clusters provides a significant improvement to particle identification when combined with the traditional measurement of the integrated charge.

Contents

List of Tables

List of Figures

ACKNOWLEDGEMENTS

I would like to thank:

Dr. J. M. Roney for patience, assistance, and encouragement;

Paul Birney and Paul Poffenberger for all the assistance in the lab;

My fellow graduate students at UVic for the friendship and the fun;

The lovely Vanessa McCumber for all the love and support; and

My parents and my sisters for dealing with my constant rambling about science.

DEDICATION

For Nana and Grandpa, whose commitment to each other for 60 years of marriage has taught me to never give up on something worthwhile.

Chapter 1

Introduction

SuperB is an e^+e^- collider experiment with the goal of exploring flavour and lepton physics. It will operate with a beam luminosity 100 times higher than any previous experiment of that type. The detector will contain several devices, one of which is known as a drift chamber.

A drift chamber is a device which uses the ionization of a gas by an incident particle to measure the trajectory and velocity of the particle. It is composed of a series of wires suspended in a gaseous medium. As a particle traverses the gas, it liberates electrons, which drift towards the subset of wires that have a positive potential applied to them causing further ionization as they approach the wire, while the ions drift away from the positive wires. The number of electrons liberated is related to the velocity of the particle, and the path that the particle follows in a magnetic field is related to the momentum of the particle. Using the measurement of the velocity and momentum, the particle's mass can be determined, and from that, it's identity.

In most drift chamber experiments, the amount of charge deposited on the wire is measured as the proxy for the number of liberated electrons (clusters). The method has problems associated with it, due to changes in the gas amplification, fluctuations in the number of secondary electrons produced by each cluster, as well as so called delta electrons: electrons liberated by the incident particle that have enough energy to cause further ionization. This thesis will explore a new technique. In addition to measuring the total charge induced on the wire as a proxy for the number of clusters, the number of clusters itself will be measured. To this end, two experiments were performed: a small cylindrical chamber was tested at the University of Victoria, and a prototype drift cell, similar to what may be used at SuperB, was tested at the

TRIUMF laboratory in Vancouver BC.

In chapter 2, the SuperB experiment will be explained in some detail, with emphasis on the drift chamber. Chapter 3 will explain the theory of drift chamber operation how energy is deposited by a particle traversing a gas, and how this can be used to identify the particle. Chapter 4 will describe the experiments done, both at the University of Victoria and at the TRIUMF laboratory. In chapter 5, the process of simulating the detectors used at UVic and TRIUMF will be discussed. Chapter 6 details the analysis done on the data, from signal to noise calculations to cluster counting and charge deposition measurement. Finally, chapter 7 will summarize the results, and chapter 8 will provide some concluding remarks.

Chapter 2

The SuperB Experiment

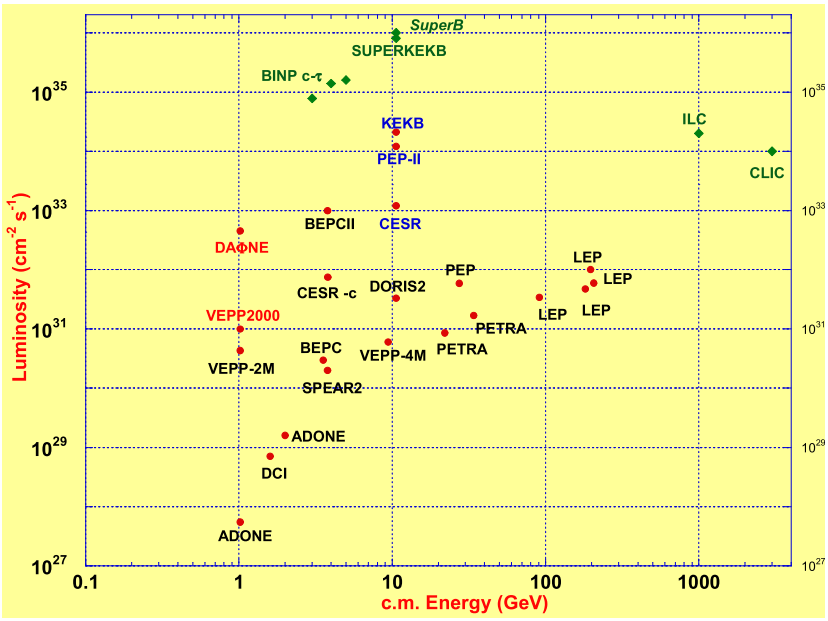

Figure 2.1: Peak luminosity vs center of mass energy for various e^+e^- colliders [2]

The SuperB experiment is an asymmetric e^+e^- collider experiment that will be built near the town of Frascati, a suburb of Rome. It is in many ways a successor to the BABAR experiment, relying on much of the expertise and even several of the components used there. The rate of particles colliding per unit area in the interaction region (known as the luminosity) at SuperB will be much higher than BABAR, $10^{36}cm^{-2}s^{-1}$ compared with BABAR's $10^{34}cm^{-2}s^{-1}$, and higher than any current e^+e^- collider project (see fig 2.1). It will operate at a lower boost than BABAR, $\beta\gamma$ of 0.24 vs 0.56, due to the requirement that the electron beam have an energy of

4.2GeV, in order to maximize the polarization time. The positron beam will have an energy of 6.7 GeV, for a center of mass energy of approximately 10GeV [2]. The goal of the experiment is to further study the flavour sector of particle physics.

SuperB will operate at the charm threshold $\Psi(3770)$ to above the $\Upsilon(4S)$ threshold. Over 5 years of operation, it will generate $75ab^{-1}$ of data, producing the world's largest sample of B, D, and τ pairs, 75 times the current statistics available elsewhere. It will be able to probe new physics in the flavour sector. A longitudinally polarized electron beam and an extended period of running at the charm threshold will allow the experiment to include an electroweak program and charm threshold studies.

The SuperB physics program consists of study of $B_{u,d}$ mesons, D mesons, and τ leptons. Spectroscopy will be performed on Standard Model particles, and precision measurements of $sin^2\theta_W$ will be made. CP and CPT on the $\Upsilon(4S)$ and $\Psi(3770)$ will be studied, as well as lepton universality. Using precision measurements on processes involving SM particles only, new physics, if within range, can be found indirectly due to its contribution of virtual particles. [3]

A recent schematic of the SuperB detector can be found in fig 2.2. The detector is based on the BaBar design, but with modifications to operate at the higher luminosity of SuperB.

The BaBar detector consists of a five layer silicon strip detector, a forty layer drift chamber in a 1.5T magnetic field, a Cerenkov detector with fused silica bar radiators, and electromagnetic calorimeter comprised of of 6580 CsI crystals, and an instrumented flux return system containing a limited streamer tube and a resistive plate chamber for K_L^0 and μ detection.

SuperB will reuse several of these components, including the steel from the flux return system, the superconducting coil, the barrel of the EM calorimeter, and the fused silica from the Cerenkov detector. The silicon vertex detector and the drift chamber, however, will be replaced, since the vertex tracker is unable to operate at SuperB's particle flux, and the drift chamber has reached the end of its life. A new forward calorimeter will be added to the design, as well as a possible forward particle ID (PID) and backward electromagnetic calorimeter. [5]

2.1 SuperB Drift Chamber

The SuperB drift chamber will have a cylindrical design, with inner and outer radii around 260mm and 800mm respectively (see fig 2.3). Its length will be approximately

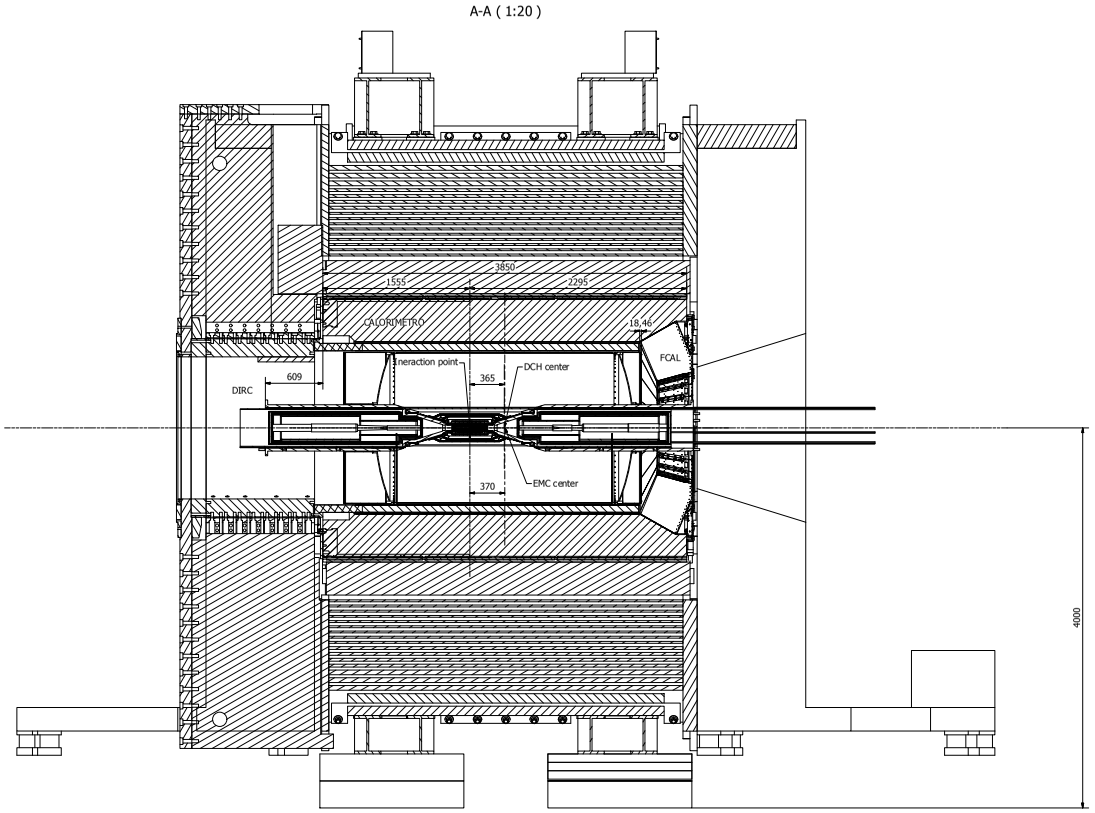

Figure 2.2: Schematic of the SuperB detector [4]

1760mm. It will be required to take momentum measurements with the same precision as BABAR, that is 0.4% for 1 GeV p_T tracks. Due to SuperB's much higher particle flux, there will be a 100 fold increase in trigger rate and luminosity related backgrounds such as radiative Bhabhas.

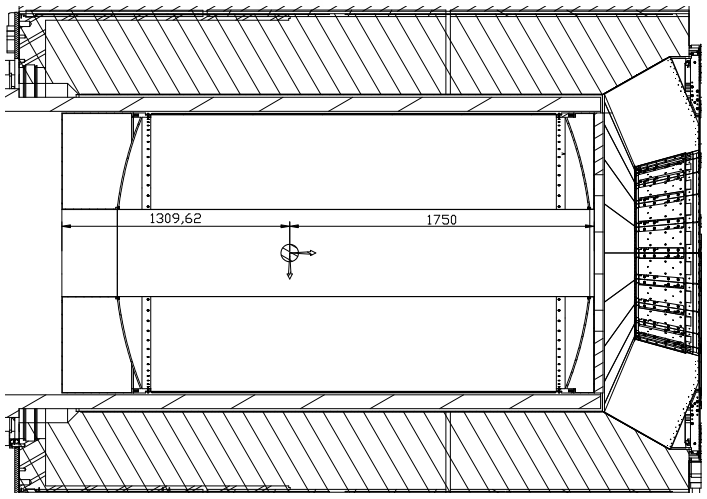

Figure 2.3: SuperB drift chamber [6]

The cell layout will be a series of rectangular cells in forty concentric layers, each cell between 10 and 20mm in size (see fig 2.4). Some of the layers will be parallel to the axis of the chamber, with the remaining 'stereo' layers at a small angle to provide measurements of z coordinates (parallel to the beampipe). Each cell will contain 1 gold plated tungsten anode wire with a diameter of 20 - 25μm, which will be tensioned to a value consistent with yield strength and electrostatic stability. The gold plating prevents oxidization while the tungsten provides the necessary strength for such a thin wire. A voltage of approximately 2kV will be applied to provide a gas gain of about 5×10^4. There will be aluminum cathode wires, the diameter of which will be chosen to to keep the surface field below 20kV/cm. They will be tensioned so that the gravitational sag of the wires will be equivalent to the anode wire. [5]

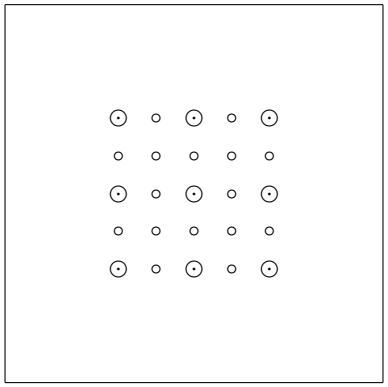

Figure 2.4: Wire arrangement for SuperB detector. ⊙ represents the anode wires and ∘ represents the cathode wires.

Chapter 3

Drift Chamber Theory

A drift chamber is a tracking device that uses the drift time of electrons produced from ionization by incident particles to measure the spatial position of the incident particle. A drift chamber is comprised of an array of wires: the anode (or sense) wires and the cathode wires. The anode wire has a voltage applied to it, which causes the ionization electrons to drift towards it while the cathode is grounded. In addition, there are field wires near the edges of the detector which help to shape the field.

In addition to measuring the spatial position of an incident particle, a drift chamber can also be used to measure the ionization caused by the particle. This ionization is related to the velocity of the particle, and can be used as a means of particle identification.

3.1 dE/dx

The formula for energy loss originally derived by Bethe and Bloch is [8]

$$\frac{dE}{dx} = 4\pi N_0 r_e^2 mc^2 \frac{Z}{A}\rho\frac{1}{\beta^2}z^2\left[ln\frac{xmc^2\beta^2\gamma^2}{I} - \beta^2 - \frac{\delta(\gamma)}{2}\right] \tag{3.1}$$

where N_0 is Avogadro's number, m is the electron mass, r_e is the Bohr radius, c is the speed of light, Z is the atomic number of the target material, A is the atomic mass, z is the charge of the incident particle, β is the velocity of the particle (v/c), γ is the Lorentz factor $(1-\beta)^{-1/2}$, I is the ionization potential of the target material, ρ is the density of the material, x is the depth into the material, in units of density times distance, and $\delta(\gamma)$ is a correction factor for relativistic particles. Since Z/A is

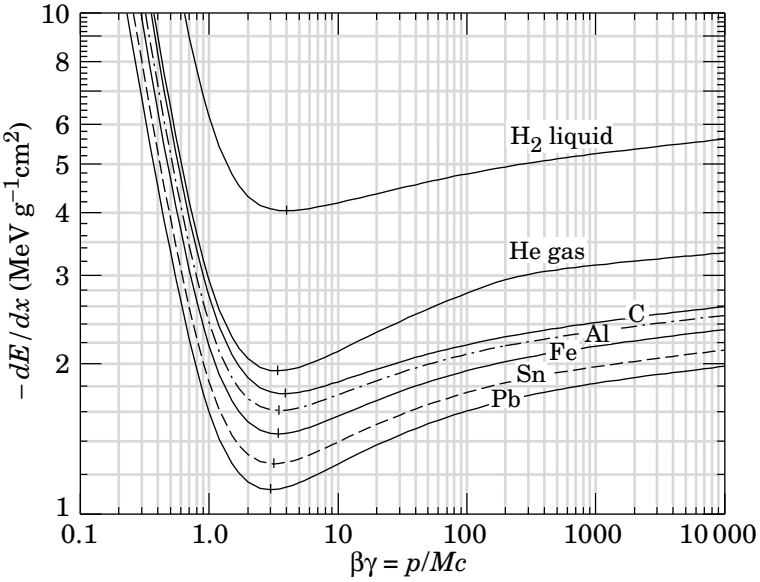

Figure 3.1: Plot of dE/dx in various media. Minimum is at $\beta\gamma \approx 4$, after which dE/dx enters relativistic rise [7]

about 0.5 in all but hydrogen and the heaviest elements, the dependence of eq 3.1 on the target medium is very weak. It varies as $1/\beta^2$ for non relativistic velocities, reaches a minimum around $\beta\gamma \approx 4$, then increases logarithmically until it reaches a plateau (see fig 3.1). This rise is caused by the transverse component of the electric field of the incident particle being proportional to γ, causing more distant collisions to become important. As the impact parameter of the collision becomes comprable to the interatomic distance, polarization effects start to become important, halting the increase and producing the plateau. The magnitude of this plateau is dependent on the density of the target material through the correction factor $\delta(\gamma)$. In solids and liquids, it is only a few percent. In gases, it can be 50%-70% higher than the minimum, and as such, gas is the practical choice for a medium to measure dE/dx. [8] [9]

The bulk of the energy lost is in the ionization of the gas. The incident particle produces primary ionization as it traverses the medium. These primary ionizations are Poisson distributed. There is a probability of high-energy transfers occurring. These high-energy transfers are known as delta rays, and they contribute to the high tail in the energy deposition spectrum (see fig 3.2). [8]

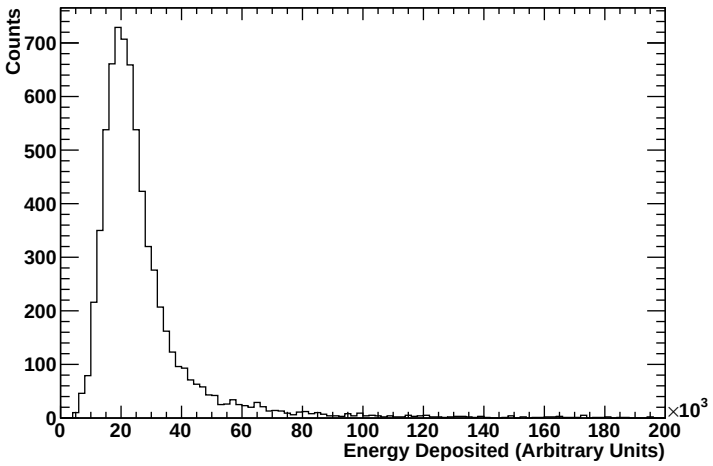

Figure 3.2: Energy deposition spectrum in a gas. Note Landau tail. Horizontal scale is 2000units/bin

3.2 Processes in Gases

As an incident particle traverses a gaseous medium, it loses energy through several processes. The first is elastic scattering, which plays an insignificant role, since the energy lost that way is so small. The second is excitation, where the gas atoms are raised to a higher energy state. The third and most important is ionization.

The number of ionizing collisions per unit length caused by an incident particle is called the primary ionization. Due to the statistical nature of the energy loss, some of the electrons from the primary ionization may have enough energy to cause more ionization. These high energy ionization electrons are known as delta rays. Due to their influence, it is useful to define the total specific ionization as the actual number of ions created per unit length. For reference, values of primary and total ionizations for minimum ionizing particles in various gases can be found in table 3.1. [10]

Primary ionization has a Poisson distribution. It is the final result of a very large number of unlikely events, the ionization collisions. The number of randomly distributed clusters K along a track of length l fluctuates around $K_0 = lN_{cl}$ (where N_{cl} is the number of clusters per unit length) with probability

$$P(K, K_0) = e^{-K_0}(K_0)^K/K! \tag{3.2}$$

When the Poisson behavior of the primary ionization is compared with the distribu-

Gas	Primary Ionization cm^{-1}	Total Specific Ionization cm^{-1}
H_2	5.2	9.2
He	4.2	8
Ar	23	94
C_4H_{10}	84	195
80% He, 20% C_4H_{10}	20.16	45.4
90% He, 10% C_4H_{10}	12.18	26.7

Table 3.1: Primary and Total ionization in various gases and mixtures, for minimum ionizing particles at 20°C and 1atm [11]

tion of the total ionization, it is clear the primary ionization is better behaved. Due to various different processes which fluctuate wildly such as δ rays (discussed below) and fluctuations in gas amplification, the statistical distribution of the energy loss is Landau distributed, with a tail towards high energy. [12]

Once the ionization occurs, several processes can occur, such as recombination, attachment, charge exchange, and absorption by the chamber walls.

Electron attachment can decrease the number of detected electrons significantly. This occurs when even a small amount of some electronegative gas such as oxygen pollutes the chamber. The high electronegativity of the pollutant allows it to absorb electrons easily, preventing them from reaching the anode wire. As such, the gas must be controlled carefully to prevent pollutants from entering the system.

Charge exchange is a process that can remove the positive ions created in the gas. When the ionization potential of the gas is greater than that of some other molecule mixed in, the molecule quenches the ion multiplication by neutralizing the ions of the chamber gas. The ionization energy is dissipated when the larger molecule disassociates into smaller fragments, and photons from radiative emissions are absorbed. [10]

3.3 Gas Multiplication

When an electron is freed in a drift chamber, it will drift towards the anode wire. As it gets closer, the electric field it feels will increase with 1/r. The closer the electron gets to the wire, the larger the electric field it experiences will be. The electron will accelerate, and eventually it will reach a point where it accelerates enough between collisions with the chamber gas that it can ionize the gas further. These newly

freed electrons will then ionize the gas around them, forming an avalanche of charge. Eventually all of the electrons will be collected on the wire.

Around atmospheric pressure, the mean free path between collisions is on the order of microns. In order to reach an energy great enough to ionize the nearby atoms, an electric field of $10^4 V/m$ is required, and as such the wire must be very thin ($\sim 10^{-3} cm$) in order to achieve this with a reasonable anode voltage.

During the avalanche process, many photons are created, some of which may be energetic enough to ionize the gas. These photons are able to travel outside the avalanche area, and can create another avalanche in a different location, causing a runaway effect known as breakdown. The photons can also reach the cathode surface, where they can create free electrons via the photoelectric effect. If an organic gas is added to the chamber gas, the photons will be absorbed. Since organic molecules have many degrees of freedom, they have large photon absorption cross sections over a wider range than the noble gases generally used in drift chambers. Using an organic additive (known as a quencher) allows the voltage on the wire to be increased (therefore increasing the gain) without breakdown occurring. Isobutane is a common choice for a quencher. [10]

3.4 Types of Drift Chamber

There are three major types of drift chamber: planar, cylindrical, and proportional tubes. In collider experiments, cylindrical chambers are used to surround the interaction region. This is what will be used at SuperB. In a traditional cylindrical chamber, half the wires are parallel to the magnetic field, and the other half are rotated by some small angle to resolve ambiguities and determine z coordinates. [10]

3.5 Tracking

The primary purpose of a drift chamber is to measure the tracks caused by ionizing radiation. If the time to distance relationship of a gas is known, then the time it takes for an electron to drift to a sense wire can be used to determine how far from the wire the track was. If multiple wires are used, then the track that the particle traversed can be reconstructed.

In the presence of a magnetic field, a charged particle will follow a curved path,

the radius of which is given by

$$R = \frac{p}{qB} \tag{3.3}$$

If a detector is permeated by a magnetic field, the tracks of the particles through the drift chamber will follow a curved path, with a radius that is proportional to its momentum in the direction perpendicular to the direction of the magnetic field.

3.6 Particle Identification

In the presence of a magnetic field, it is possible to measure the momentum of a track based on its radius of curvature. If the ionization is also measured along this track, it is possible to measure the velocity of the particle. With the momentum and velocity of the particle now known, the mass can be deduced. Since the mass of a particle is unique to a particle, identification is possible.

When the momentum and ionization are measured, this results in a point on a plot of ionization vs momentum, as in fig 3.3. If only one curve is within the uncertainties, the particle can be identified. Since the distribution of total ionization is Landau, however, the uncertainties can be very large, causing them to intersect two or more different particle curves, making particle identification difficult.

3.6.1 Charge Measurement

The best method currently used for particle identification in drift chamber experiments is called the truncated mean. In this method, the charge deposited on the wire is integrated, removing any cluster information, resulting in a number that is proportional to the total ionization. This integrated charge is sampled many times along a track, generally by having a number of layers of drift cells. For each track, the largest 20%-40% of measurements are discarded, and the mean of the remaining measurements is taken. The goal of this is to remove the high energy tail of the Landau distribution, which generally consists of large pulses from delta electrons. Using this method results in a significant improvement in particle separation over simply measureing the total ionization.

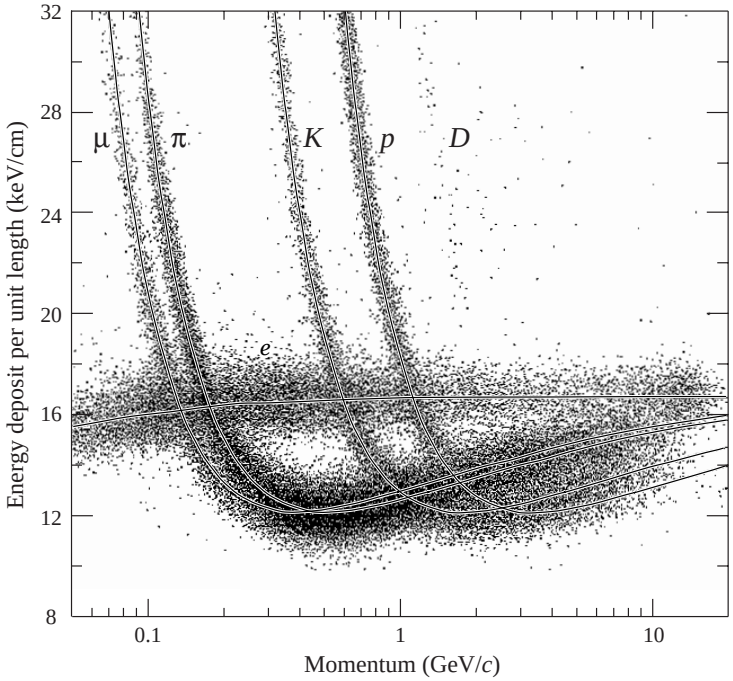

Figure 3.3: Ionization energy loss vs particle momentum for different particle species. [7]

3.6.2 Cluster Counting

An alternative method of particle identification involves counting the primary ionization rather than the total ionization. The primary ionization has a Poisson distribution rather than Landau, and as such, does not suffer from the problems of a high energy tail.

In order to perform cluster counting, there are several requirements that must be met. It must be possible to single out electrons from a single ionization act. Pulses from different clusters must have a small chance of overlapping in time, while pulses from the same cluster must all arrive simultaneously. Due to the incompatibility of these requirements, some optimal condition must be found. [13]

3.7 Gas

In order to get precise momentum measurements, it is necessary to minimize multiple scattering. Since it is a low Z gas, helium is a good choice, and has been used in other drift chamber experiments, including BaBar. Incidentally, helium also has

properties that make it useful for cluster counting. It has a high ionization potential of 24.5 eV, compared with 15.7 for argon. This leads to smaller primary and total ionization, and therefore a larger gap between clusters. Its slow drift velocity amplifies cluster separation in the time domain. The high ion mobility of helium clears up the space charge region quickly. Helium has a greater diffusion coefficient than argon, which can be counteracted by a small amount of quencher being mixed in. [13]

3.7.1 Quencher

In practice, drift chambers do not use pure gases. A quencher, generally a polyatomic organic molecule, is added. These molecules have many degrees of freedom, which allow them to absorb energy, such as photons from radiative deexcitation, or from the avalanche process itself. The photons are thus prevented from ionizing the gas at other locations and producing a second avalanche. The gain of the chamber can then be increased without breakdown occurring. Quenchers also reduce the drift velocity and decrease the diffusion. A common choice for a quencher gas is isobutane. [10]

Chapter 4

Experimental Apparatus

4.1 UVic Chamber

The chamber setup at the University of Victoria consisted of a 2.7 meter long copper tube with a diameter of 2cm. Inside the tube, a tungsten wire with a diameter of $20\mu m$ was suspended. Fittings at each end of the tube allowed gas to be passed into the chamber. At one end, the wire was connected to a high voltage power supply to raise the voltage of the wire to 1500V-1900V. At the other end, the wire was connected to a Wentec commercial preamp. A circuit diagram of the chamber can be found in fig A.1. The preamp was connected to a Tektronic TDS 404B scope.

The gas system consisted of a canister of 80% helium, 20% isobutane and a canister of pure helium, each connected to an Edwards 825 series B flow controller, then combined together. This allowed any mixture of helium and isobutane to be put into the chamber. The gas then flowed through a filter to remove any particulate matter that may have entered the tubes, and finally entered the chamber. Before data was taken with the chamber, it was flushed with ten volumes of gas to remove any oxygen that may have leaked in, which could degrade the measurement.

The chamber was tested with 80% helium, 20% isobutane and 90% helium, 10% isobutane. Table B.1 summarizes the wire voltages for these gas mixtures as well as the surface field (from simulation) on the wire. The gas gain in the system was estimated in section 6.2.3.

For triggering on cosmic rays, a pair of scintillators was used. These where placed above the chamber, as seen in fig 4.2. The output of the photomultiplier tubes connected to the scintillators was split, with one branch of each going to a coincidence

unit, and the other going to the oscilloscope. The coincidence of the two scintillators was used to trigger the scope. A photograph of the setup can be found in fig 4.1.

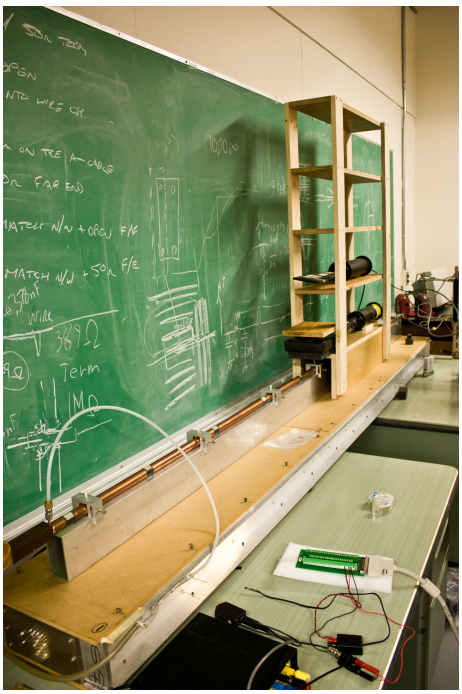

Figure 4.1: Photograph of UVic chamber

The data acquisition for the system was set up to record the traces from both scintillators and the chamber upon coincidence of the scintillators and a pulse in the chamber that was above some threshold. This made it possible to record data when a cosmic ray muon travelled through both scintillators and the chamber. Sample traces from the chamber can be found in figure 4.3.

4.2 TRIUMF Testbeam

In November of 2011, a test chamber, serving as a single wire prototype of the SuperB drift chamber, was setup in the M11 beam at TRIUMF. The beam consisted of muons, pions, and electrons, and data was taken at various momenta from 120MeV/c to 400MeV/c, as well as three different gas mixtures: 80% helium, 20% isobutane; 90% helium, 10% isobutane and; 95% helium, 5% isobutane. The momentum range was chosen such that the separation of muons and pions is similar to the separation of pions and kaons at higher momenta.

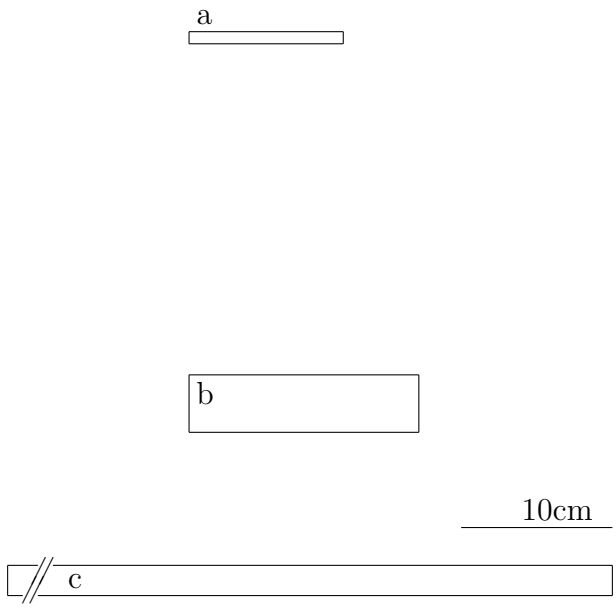

Figure 4.2: Schematic of UVic chamber showing upper trigger scintillator (a), lower trigger scintillator (b), and drift chamber (c) (not to scale). Photomultiplier tubes and support structure have been omitted for simplicity.

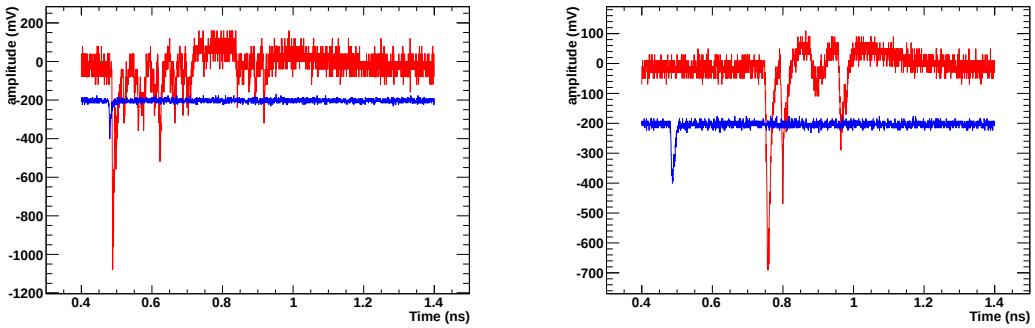

(a) 80% Helium, 20% Isobutane

(b) 90% Helium, 10% Isobutane

Figure 4.3: Sample pulses from UVic chamber. Red is the drift chamber, blue is the lower scintillator. Resolution is 1ns/bin

The experimental setup consisted of the chamber in the center on a cart which allowed it to be moved so that all but one of the five windows on the chamber would be in the center of the beam. The cart was also able to pivot so that the chamber could be set at an angle with respect to the beam. This can be seen in fig 4.4.

The chamber used in the testbeam had a wire arrangement designed to mimic the possible SuperB chamber (see fig 4.6). A central 25μm gold plated molybdenum anode wire was surrounded by eight 80μm gold plated aluminum cathode wires. In addition, another set of gold plated aluminum field wires was used to simulate an infinite detector. The anode wire was tensioned to 27g, while the cathode and field wires were tensioned to 87g. The potential applied to these wires was changed as the gas mixture was changed. For 90/10 gas, the anode wire was at 1800V and the field wires were at 1023V. Values for other gases can be found in table B.1 A preamplifier prototype designed at the University of Montreal was used (see fig A.3), as well as the same Wentec preamp used on the Uvic chamber. A diagram of the circuit can be found in fig A.2. For several runs, the 390Ω resistor was replaced with a 1.5MΩ resistor, so that the chamber was unterminated. A sample pulse can be found in fig 4.5

A pair of scintillators, one immediately outside the beam aperture, and one as far away from that as possible while still being in the beam, was used for triggering as well as particle identification. The time of flight (TOF) for a particle to travel from one scintillator to the other was used to determine what particle travelled through the drift chamber in a given event. A plot of the TOF distribution for 140MeV/c particles can be found in fig 4.7. There are clear peaks for each particle. Each scintillator had

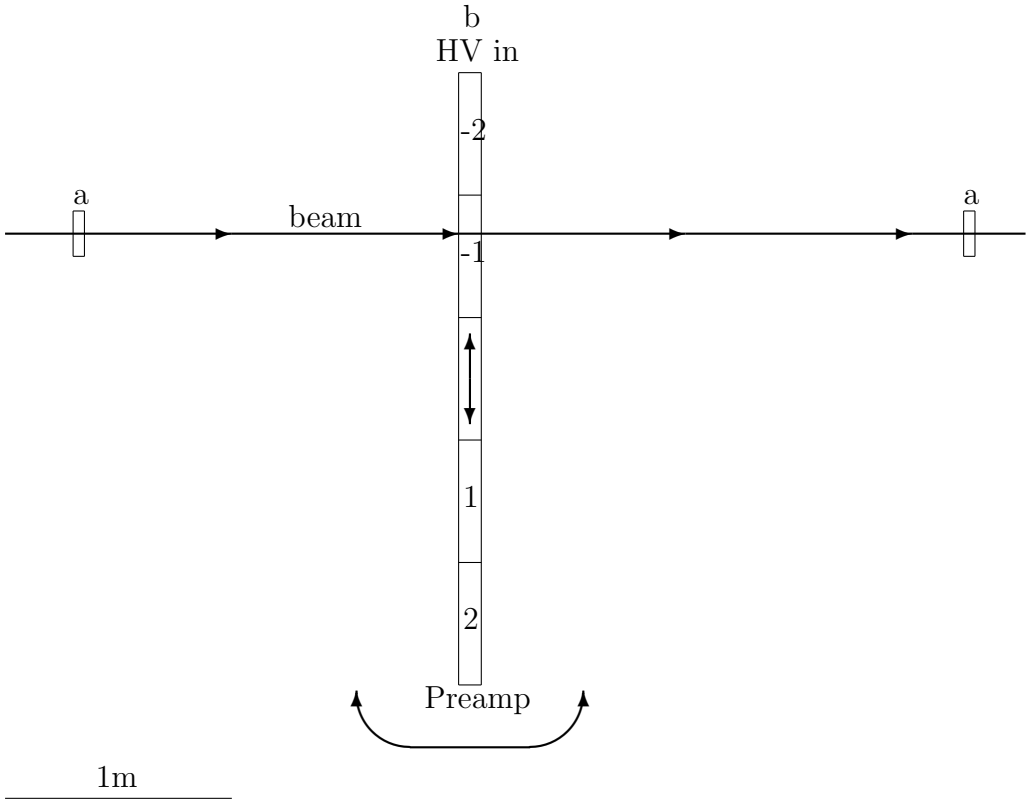

Figure 4.4: Schematic of TRIUMF testbeam showing the TOF scintillators (a), and the prototype drift chamber (b). The numbers indicate which window was in use in a run.

two preamplifiers attached to it. A trigger consisted of a coincidence of all four PMTs. Despite the fact that a straight line between the scintillators must pass through the drift chamber, approximately 40% of the events had no pulse in the drift chamber. These events are likely due to particles scattering off the support structure of the chamber.

A photo of the TRIUMF testbeam can be found in fig 4.8, and a schematic in fig 4.4. For reference, the chambers were enumerated such that the central window was 0, the windows towards the HV end counted down and the windows towards the preamp end counted up.

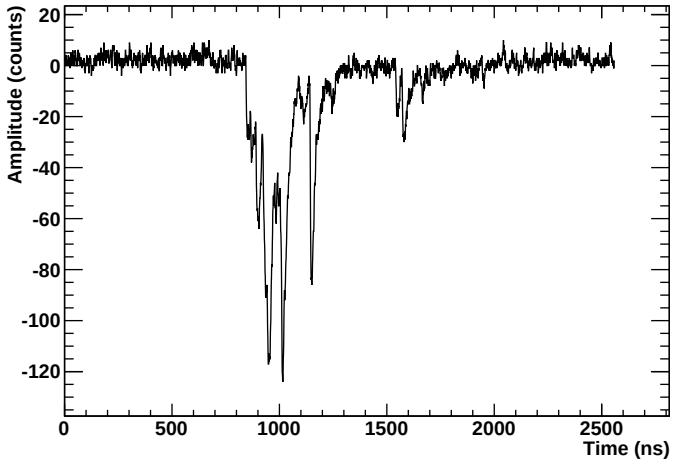

Figure 4.5: Sample Pulse from TRIUMF testbeam. Beam was at 140MeV/c, and filled with 90/10 gas. The preamp designed in Montreal was used. Resolution is 0.5ns/bin

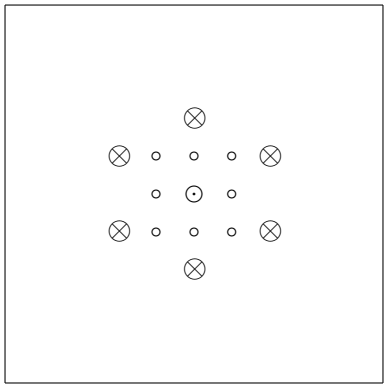

Figure 4.6: Wire arrangement in TRIUMF testbeam. $\odot$ represents the anode wire, $\circ$ represent the cathode wires, and $\otimes$ represent the bias wires.

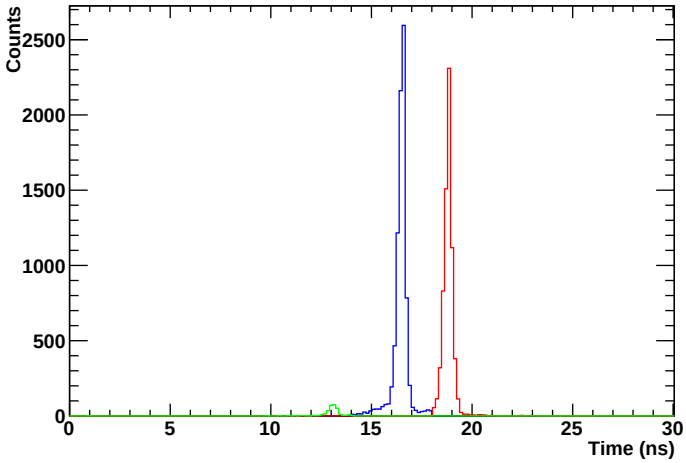

Figure 4.7: Time of fight of particles at 140MeV/c: green is electrons, blue is muons, and red is pions. Horizontal binning is 0.15ns/bin

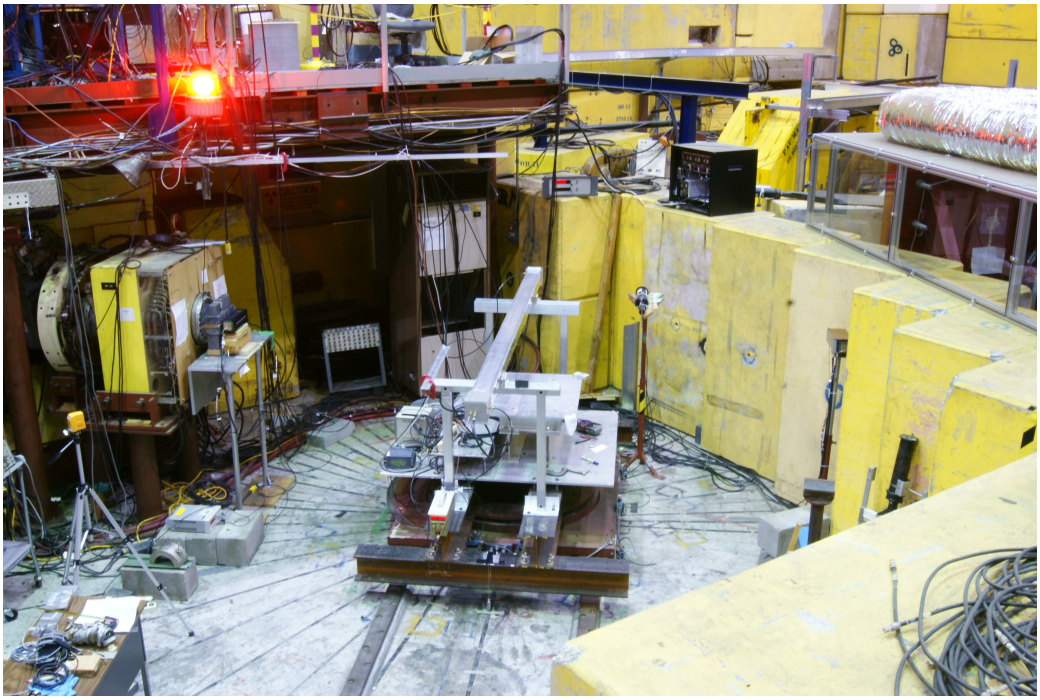

Figure 4.8: Photograph of TRIUMF testbeam

Chapter 5

Simulation

Garfield is a program designed to simulate gaseous detectors. The various parameters of a detector can be input into the program, such as the geometry of the detector, the gas mixture used, and the impulse response of the electronics. Using these, it is able to simulate the performance of the detector, calculate electron and ion drift velocities and paths, produce signals, and much more. In this analysis, it was used as a basis for comparison to the real signals produced in the UVic and TRIUMF based experiments.

5.1 Tuning UVic Simulation

In order to measure the impulse response of the preamplifier, a 12pF capacitor was connected to it. A step voltage was applied to the capacitor. This spike in voltage caused a spike in charge on the capacitor which would be very small, simulating a delta function. The output from the capacitor was the impulse response, seen in fig 5.1. This response was normalized to a peak of 1, and fit to a Gaussian function. This fit function was then used as the preamp impulse response in Garfield.

The simulated signals were tuned to match the real signals. To accomplish this, the signal and noise distributions for the real data were plotted (see section 6.2.4). The signal and noise distributions of the simulation were then scaled to match the real data (see fig 5.2). The data was simulated using 1GeV/c muons. The UVic chamber, however, had no ability to select the momentum of the cosmic rays, and as such had a distribution of momenta, which causes some discrepancies between data and simulation.

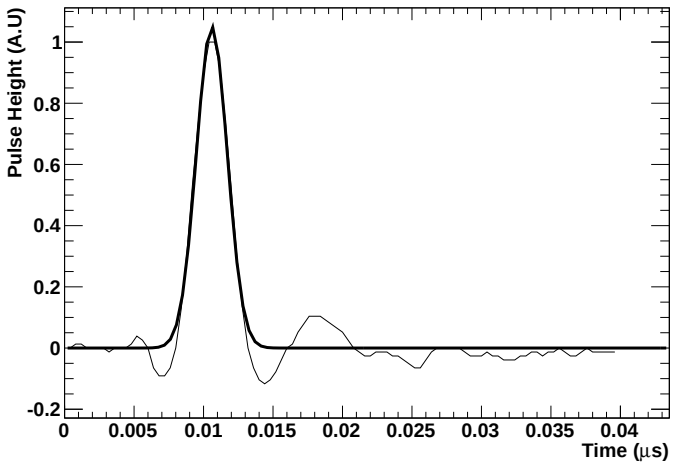

Figure 5.1: Impulse response of Wentec preamp, used in UVic chamber

Garfield works by first computing the raw current induced on the wire as in fig 5.3(a). This raw signal is then convolved with the preamp impulse response to yield fig 5.3(b). Finally, the noise is added to get the final signal, as in fig 5.3(c).

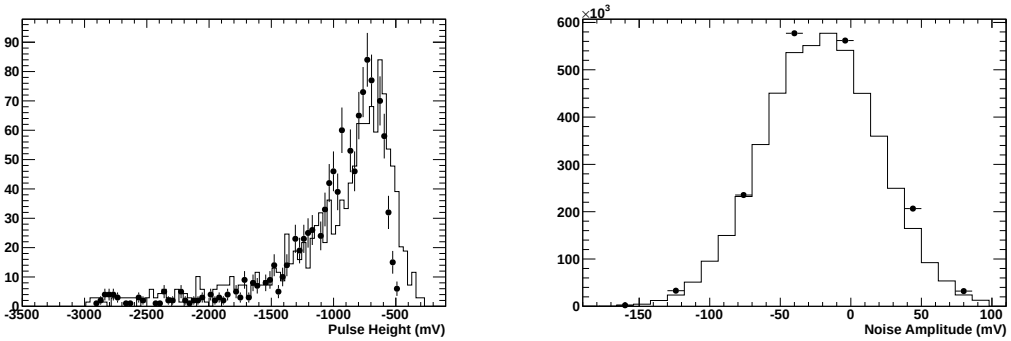

Figure 5.2: Real and Simulated data, UVic chamber: (a) Distribution of pulse heights, horizontal scale is 34mV/bin. (b) Distribution of noise, horizontal scale is 3.2mV/bin. • represents real data, - represents simulated data. Horizontal error bars are defined by the bin width, vertical error bars by the square root of the number of entries in the bin.

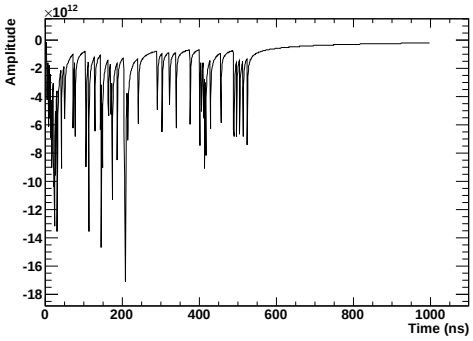

(a) Raw signal

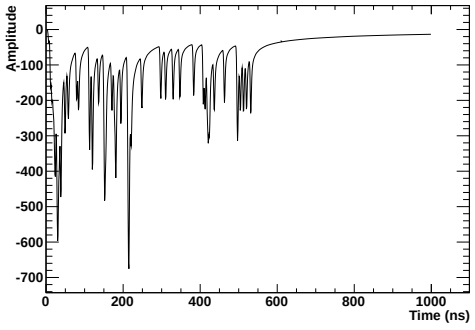

(b) Preamp added

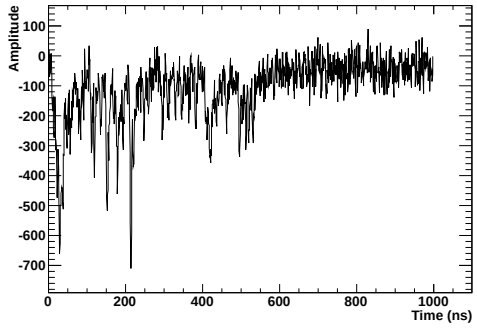

(c) Final signal

Figure 5.3: Simulation of signal in Garfield for 1GeV/c muons (bin width is 1ns)

5.2 Tuning TRIUMF Simulation

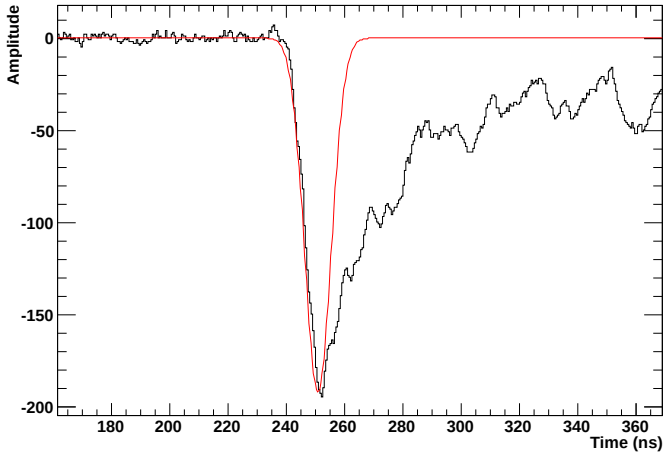

Figure 5.4: Generation of TRIUMF preamp function. Black line is the actual data, red is the simulated preamp impulse response.

The response of the preamp used in the TRIUMF testbeam was obtained by looking at the pulses. By assuming that each cluster in the pulse is the result of a small deposit of charge on the wire being amplified by the preamp, the response could be estimated by fitting a Gaussian function to the leading edge of one the pulses, as demonstrated in fig 5.4. This was repeated for six pulses, and the average of the fits was taken. The resulting transfer function can be found in fig 5.5.

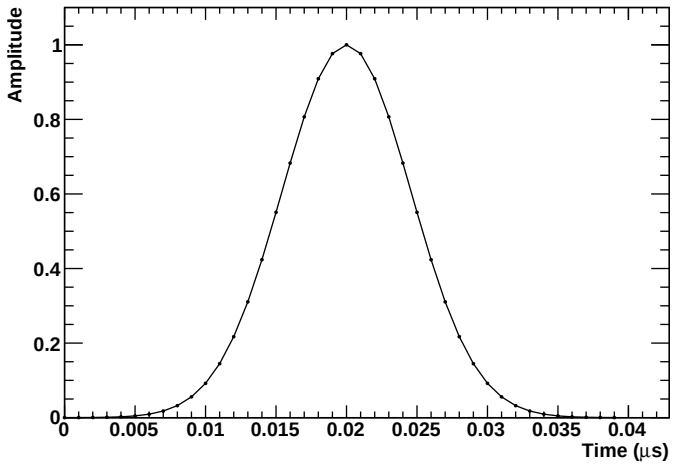

Figure 5.5: Preamp impulse response for TRIUMF data

Signal pulses were generated in Garfield using the cell arrangement of the TRIUMF chamber (see fig 4.6) and a 90/10 gas mixture. Rather than tune based on the signal distribution, the simulation was tuned to have the same truncated mean (see section 6.3.4) as the real data, then the noise was added. A sample signal from the simulation can be found in fig 5.6. There is a noticable difference between the real and simulated data however, the quanties of interest, such as the seperation of the cluster distributions and the truncated mean are similar, as described in chapter 6.

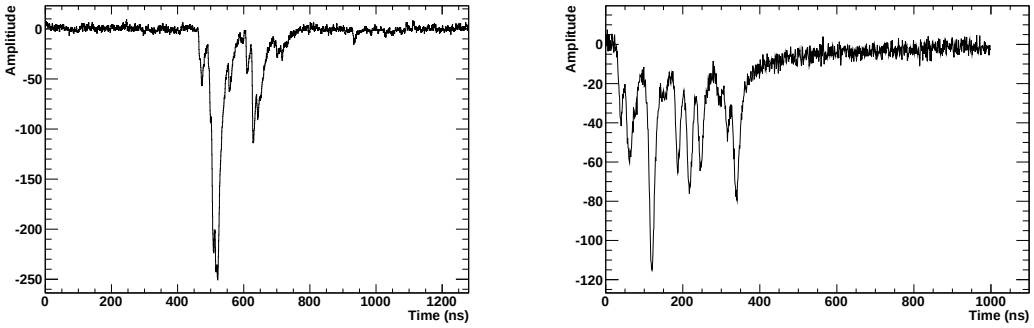

(a) Real trace, bin width of 0.5ns (b) Simulated trace, bin width of 1ns

Figure 5.6: Real and Simulated traces, TRIUMF chamber.

Chapter 6

Analysis

6.1 Cluster Counting Algorithm

In order to detect the clusters, the following algorithm was applied to a waveform:

$$a_i = v_i - \frac{\sum_{j=1}^{n} v_{i-j}}{n} \tag{6.1}$$

where v_i is the amplitude of a the ith time bin. This algorithm subtracts the average of the n bins preceding a given bin. The result, a_i, will have a large value when there is a large increase in the pulse height. If this value is above some threshold, a cluster is said to have been detected, provided that the previous bin was below the threshold. The requirement that the previous bin be under the threshold prevents a cluster from being counted multiple times. This threshold must be chosen carefully to optimize the algorithm.

In addition to the threshold, the number of bins averaged over can also be adjusted to optimize the algorithm.

An example of the cluster counting algorithm applied to a waveform can be seen in figure 6.1

6.2 UVic Chamber

6.2.1 Leak Rate

The first analysis done on the UVic chamber was to determine the leak rate, in order to minimize the amount of gas used. Once the chamber was flushed with fresh gas, a

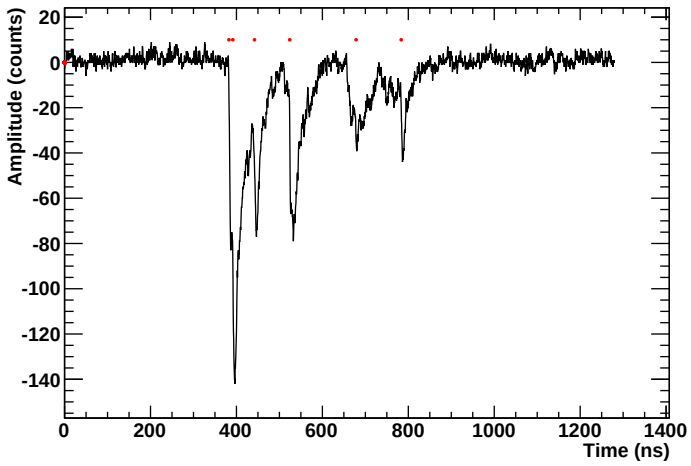

Figure 6.1: Example of cluster counting algorithm applied to a waveform with a threshold of -8, n=5. Red dots represent where a cluster is detected. Bin width is 0.5ns

series of waveforms in the chamber was recorded at ten minute intervals for 24 hours. The mean pulse height each ten minute sample was plotted against time (see fig 6.2), and the data was fitted to this simple function:

$$A_0 \qquad t < t_1 \tag{6.2a}$$

$$A_0\,[1 - L(t - t_1)] \quad t > t_1 \tag{6.2b}$$

The results of the fit can be found in table B.2

Using these data, the flow rate of fresh gas into the chamber could be controlled to maintain the best pulse heights, while minimizing the amount of gas used.

6.2.2 Time Distribution

The time distribution of pulses in the UVic chamber was determined. The time difference between when the lower scintillator (see fig 4.2) triggered and when the drift chamber triggered was calculated. The distribution can be found in fig 6.3 for 80/20 and 90/10 gas mixtures. As evident from the figures, there is a slightly larger tail in the 90/10 mixture. This may be related to the difference in gas mixture itself, or the different voltage applied to the wire.

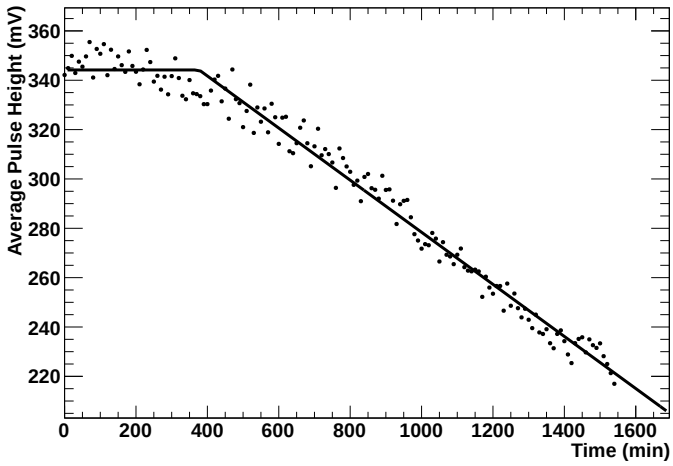

Figure 6.2: Example of leak rate measurement

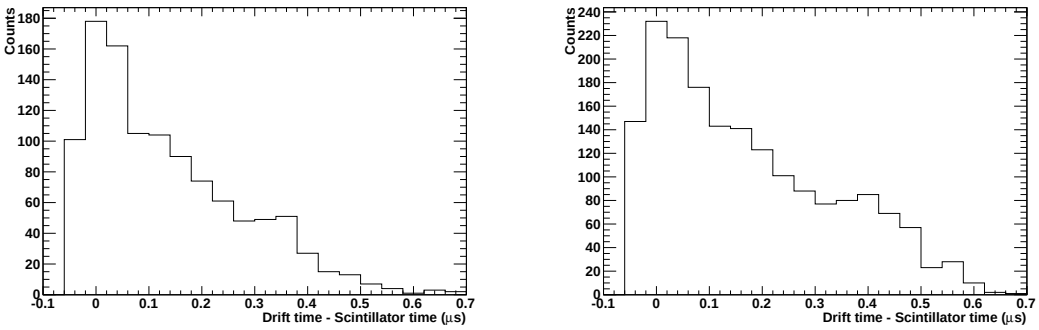

(a) 80% helium, 20% isobutane

(b) 90% helium, 10% isobutane

Figure 6.3: Time distribution for UVic chamber. Horizontal scale is 30ns/bin

6.2.3 Gain Estimation

To estimate the gain of the chamber, the response of the preamp to a known amount of charge was needed. To get this value, a step function with some voltage was applied to a 12pF capacitor which was connected to the preamp. The voltage applied to the capacitor was varied, and the response of the preamp was measured. The charge deposited on the capacitor by the voltage spike was calculated using the following:

$$C = \frac{Q}{V} \tag{6.3}$$

where C is the capacitance, Q is the charge, and V is the voltage applied. Using this, a graph of the charge on the preamp vs. the output voltage of the preamp was

plotted as seen in fig 6.4, and fit to a line.

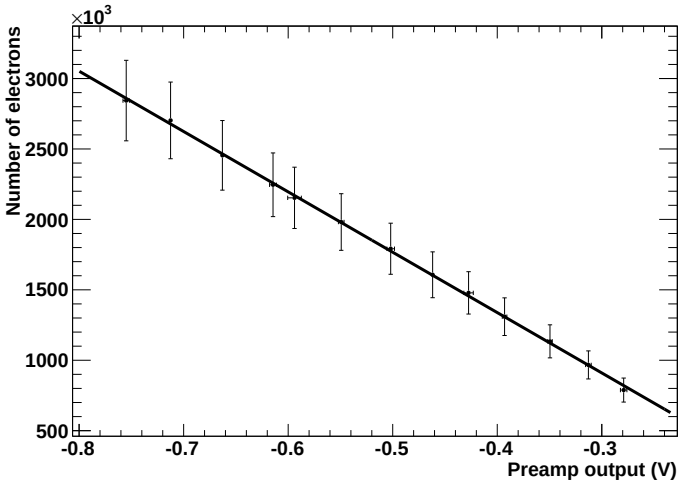

Figure 6.4: Charge vs Preamp Voltage. Error bars are dominated by tolerance of the 12pF capacitor, and therefor there is large correleated error between points.

Garfield was used to determine how many electrons would be produced in either 80/20 or 90/10 gas for a 1GeV muon travelling through the center of the wire. From the real data for these gases, the integral of the waveforms occuring less than 100ns after the lower scintillator trigger was measured and converted into the number of electrons deposited on the wire using the calibration curve in fig 6.4. Using this value and the number of electrons produced by the incident particle, the gas gain of the chamber was estimated. These values for 80/20 and 90/10 gas mixtures are summarized in table 6.1

Gas	Integral of waveforms	Number of electrons deposited on wire	Initial number of electrons from 1GeV muon (Garfield)	Gain estimate	Anode surface field (V/cm)
80% He, 20% C_4H_{10}	-1.19×10^4	4.841×10^7	64.53	7.5×10^5	2.82×10^5
90% He, 10% C_4H_{10}	-6.86×10^4	1.14×10^8	35.35	3.3×10^6	2.38×10^5

Table 6.1: Gas gain calculation

It should be noted that this is only an estimate of the gain produced by the gas.

6.2.4 Signal to Noise

Noise Distribution

The triggering in the UVic chamber caused there to be a portion of each waveform that contained no signal. This 'pretrigger' region was used to study the noise. The pulse heights from the pretrigger were histogramed (see fig 5.2), which shows the digital nature of the data.

Signal Distribution

The signal distribution was measured by finding the lowest pulse height value in a waveform and adding it to a histogram. The distribution can be found in fig 5.2.

6.2.5 Cluster Counting

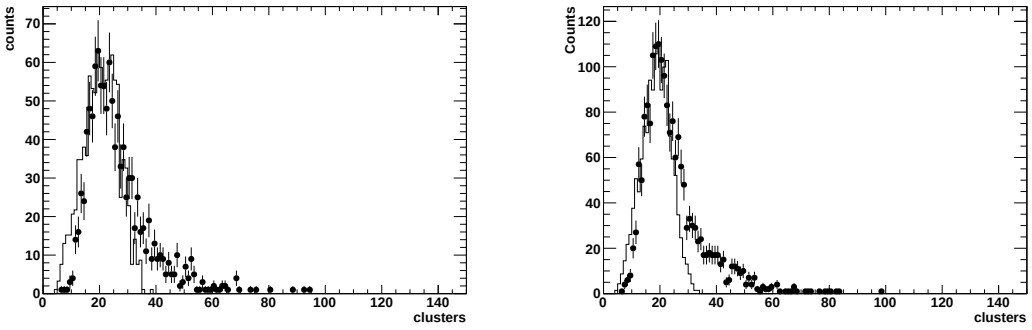

(a) 80% helium, 20% isobutane, threshold of -60 (b) 90% helium, 10% isobutane, threshold of -30

Figure 6.5: Cluster Distributions in UVic data. • represents real data, - represents simulated data. n=5 for both plots. Horizontal scale is 1 cluster/bin

Cluster distributions were produced using the UVic data for two gas mixtures: 80% helium, 20% isobutane and 90% helium, 10% isobutane. Despite the lack of particle identity information, there was still some information that could be gleaned from these. From fig 6.5, it is evident that the simulation and experiment produce similar results, with the exception of a tail towards higher cluster numbers in the experimental data, which is likely because the simulation used 1GeV/c muons, whereas the energy of the cosmic ray muons has a soft component with a lower β which would produce more clusters. Fig 6.6 shows a scatter plot of the number of clusters vs the

integrated charge on the wire. There is a clear correlation between these variables, which indicates the value of continuing to study cluster counting.

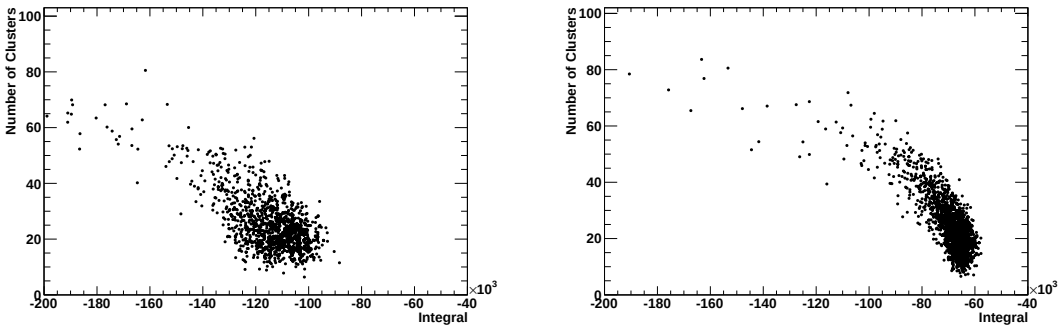

(a) 80% helium, 20% isobutane, threshold of -60 (b) 90% ielium, 10% isobutane, threshold of -30

Figure 6.6: Number of clusters vs integral for UVic data. n=5 for both plots. Horizontal scale is 1600 units/bin, vertical scale is 1 cluster/bin.

6.3 TRIUMF chamber

6.3.1 Noise Distribution

In the TRIUMF testbeam, there were a certain number of empty events resulting from scattering of particles off the support structure. These events were used to measure the noise in the drift chamber.

In each empty event, the RMS and mean of the waveform were calculated. These were each added to different distributions. The distribution of means gives the pedestal, and distribution of the RMS values gives the noise. Sample noise and pedestal distributions can be found in fig 6.7.

6.3.2 Signal Distribution

To find the signal distribution, the pedestal and noise must be removed.

The empty events were removed before determining the signal distribution. In each event, the pedestal value was subtracted from the amplitude of each time bin. Bins with a value less than three times the RMS of the noise were removed, and the mean of the remaining bins was calculated. This mean was added to a histogram for the whole data run. A sample of this distribution can be found in fig 6.8.

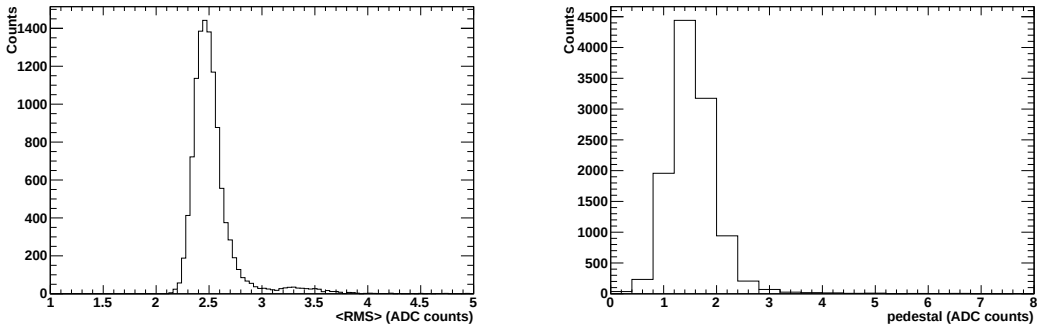

(a) Noise, RMS=2.532, 0.04 ADC counts/bin (b) Pedestal=1.592, 0.4 ADC counts/bin

Figure 6.7: Noise and pedestal distributions for TRIUMF testbeam

Table B.3 summarizes the signal and noise values for runs at various momenta and windows. The table shows that the windows closest to the preamp generally had better noise performance.

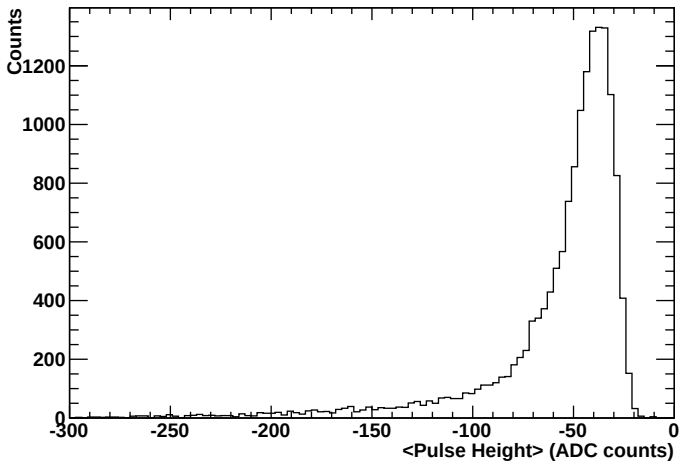

Figure 6.8: Signal distribution for TRIUMF testbeam. Mean is -57.07, RMS is 36.43, 3 ADC counts/bin

6.3.3 Cluster Counting

Cluster distributions were produced for muons and pions for various values of the threshold and n. An example of one of these distributions for muons and pions can be found in fig 6.9(a), along with a set of cluster distributions produced with simulated data in fig 6.9(b). Note the difference in the distributions: There are more clusters in

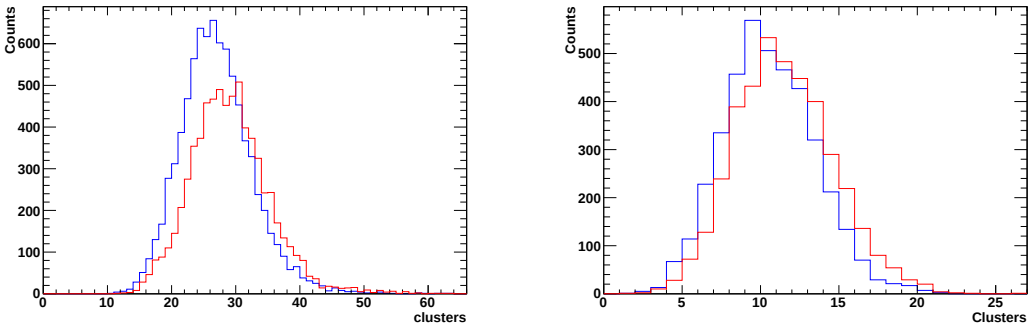

(a) Real data. (threshold of -5, n=7)

(b) Simulated data.(threshold of -9, n=7)

Figure 6.9: Cluster distributions for TRIUMF data. Muons are in blue while pions are in red. Beam is at 140MeV/c and intersects window 1, 90/10 gas used. For means and RMS values, see table B.6. Horizontal scale is 1 cluster/bin.

pions than in muons in both the real and the simulated data. It is worth noting that these distributions are Poisson, as expected for clusters. The values of the threshold and n were optimized using the process described in the next paragraph.

The resolving power was used to maximize the ability to separate particles:

$$\Delta_{Resolving\ power} = \frac{\bar{\pi} - \bar{\mu}}{\sqrt{\sigma_\pi^2 + \sigma_\mu^2}} \tag{6.4}$$

where $\bar{\pi}$ and $\bar{\mu}$ are the mean of the pion and muon cluster distributions, and σ_π and σ_μ are the RMS. For a given run, the threshold and number of bins averaged over was varied, and the values that produced the best value of the resolving power were chosen. In figure 6.10, the results of this optimization are presented. As the threshold is decreased from the optimal value, the algorithm begins to count noise fluctuations as clusters, thus degrading the result. Conversely, as the threshold is increased, the result is degraded because the algorithm is missing clusters. For low values of n, the result is degraded since the average is only sensitive to a few bins, causing the averaging part of the algorithm to fluctuate too much, whereas for large n values, the average could now include whole clusters in it, reducing the difference and deteriorating the result. The results of this optimization for other data can be found in table B.4.

The ability to resolve muons and pions was generally the best in the window closest to the preamplifier, which is consistent with the signal to noise being the highest in that window. The best resolving power found was for 140MeV/c at window 1. The

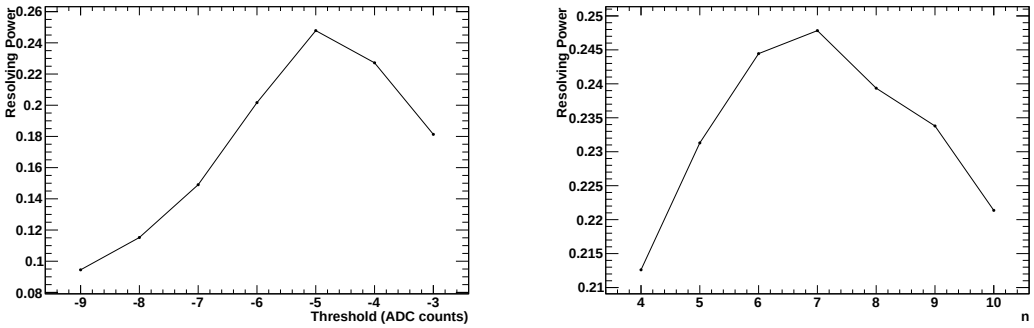

(a) Threshold (b) n

Figure 6.10: Optimization of cluster counting parameters for 140MeV/c particles in 90/10 gas in window 1.

resolving power was 0.248 in this run, based on a single wire.

There was significant degradation of the resolving power as the momentum increased, due to the distributions of the number of clusters getting closer together for muons and pions. Table 6.2 shows the number of clusters expected from pions and muons for various momenta from simulation. As the momentum increases, the difference in number of clusters decreases, reducing the ability to distinguish between the particles.

Momentum	Muons (cm^{-1})		Pions (cm^{-1})		
(MeV/c)	$\bar{\mu}$	σ_μ	$\bar{\pi}$	σ_π	$\bar{\pi} - \bar{\mu}$
140	15.87	3.95	19.43	4.33	3.56
180	14.06	3.71	16.23	3.97	2.18
200	13.6	3.67	15.26	3.87	1.67
225	13.2	3.61	14.38	3.73	1.18
250	12.87	3.46	13.8	3.62	0.93
275	12.77	3.49	13.43	3.58	0.66

Table 6.2: Expected number of clusters for various momenta, from simulation

For comparison, the same optimization was carried out on the simulated data. Fig 6.11 shows the optimization of the resolving power for a simulation of window 1 of the test chamber at 140MeV/c in 90/10 gas. The optimization parameters were larger than the real data. The resolving power of 0.225 was close to that of the simulated data.

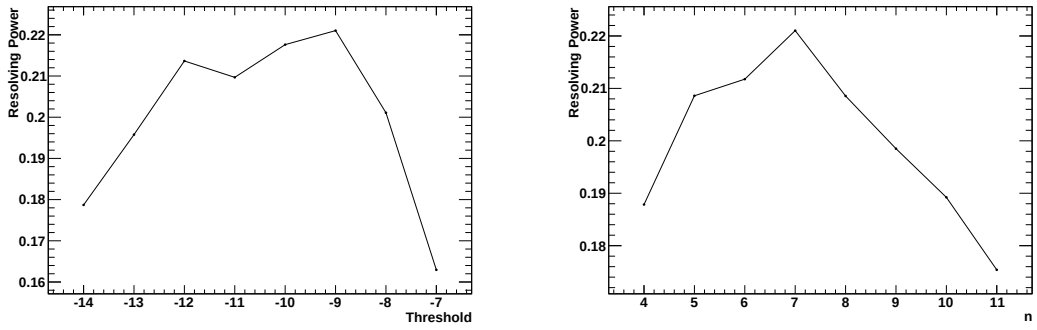

(a) Threshold (b) n

Figure 6.11: Optimization of cluster counting parameters for simulation of 140MeV/c particles in 90/10 gas in window 1.

6.3.4 Truncated Mean

As a comparison to the cluster counting analysis, a truncated mean analysis was done. Forty events of the same particle were grouped together in a combined event to simulate the forty layers of a real drift chamber. Of these forty events, the 30% with the highest integrated charge were discarded (12 events), and the mean of the remaining events was calculated. The distribution of the truncated mean can be found in fig 6.12(a) for data at window 1 of the chamber at 140MeV/c, and the results of the simulation can be found in fig 6.12(b). The simulated data and the real data line up well, since the simulated data was tuned to match the real data. Table B.5 summarizes the results for many runs, including the resolving power. The resolving power for the truncated mean corresponding to window 1 at a momentum 140MeV/c is 1.91.

6.3.5 Comparison of Cluster Counting and Truncated Mean

From section 6.3.3, the maximum resolving power achieved through cluster counting was 0.248, based on one wire, while from section 6.3.4, the resolving power from applying the truncated mean to the same data is 1.91 based on 40 wires. To compare these, the cluster counting result of 0.248 is multiplied by $\sqrt{40}$ so that it is equivalent to data taken from 40 wires. This results in a resolving power of 1.57.

The ability to distinguish muon and pions at 140MeV/s in 90% helium 10% isobutane is much better for the truncated mean than it is for cluster counting, at least with the algorithm described in section 6.3.3 and with the noise environment for these

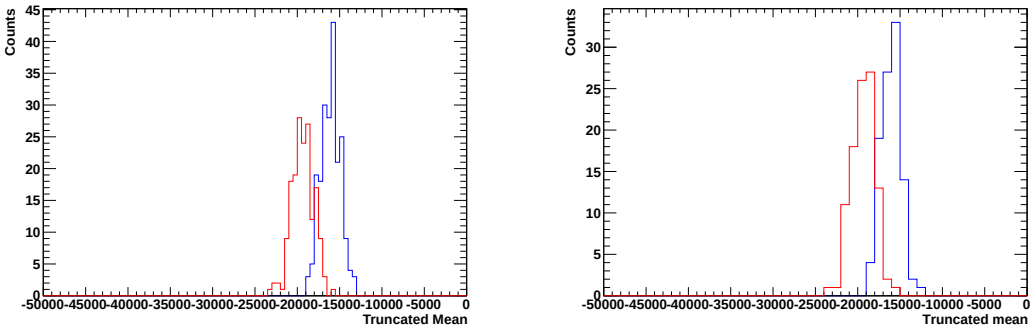

(a) Real data. (b) Simulated data.

Figure 6.12: Truncated mean distribution for 140MeV/c particles in 90/10 gas at window 1. Muons are in blue, while pions are in red. For means and RMS values, see table B.6. Horizontal scale is 500 units/bin.

tests.

6.3.6 Combined Approach

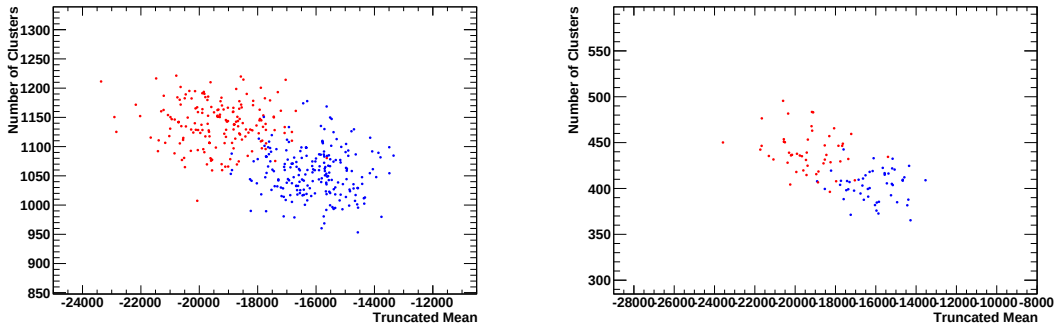

(a) Real data. (b) Simulated data.

Figure 6.13: Truncated mean vs Number of clusters for 140MeV/c particles in 90/10 gas at window 1. Blue is muons, red is pions. For means and RMS values, see table B.6. Horizontal scale is 500 units/bin, vertical scale is 1 cluster/bin

The ability to separate muons and pions was not improved with cluster counting alone in this setup and its noise, at least not with the algorithm described in eq 6.1. As such, the effect of combining cluster counting and the truncated mean was explored. Fig 6.13(a) shows a plot of the truncated mean vs. the number of clusters in the combined event. As evident from the figure, there is a separation between muons and

pions for this data as well as a correlation between the number of clusters and the integral. To quantify this separation, a likelihood method based on a two dimensional Gaussian function was used. The likelihood that a combined event was a muon was defined by

$$L_\mu^i = \frac{1}{2\pi\sigma_{N_{cl}^\mu}\sigma_{Q^\mu}} e^{-\left[\frac{\left(N_{cl}^i - \bar{N_{cl}^\mu}\right)^2}{2\sigma^2_{N_{cl}^\mu}} + \frac{\left(Q^i - \bar{Q^\mu}\right)^2}{2\sigma^2_{Q^\mu}}\right]} \tag{6.5}$$

where $\bar{N_{cl}^\mu}$ and $\bar{Q^\mu}$ are the mean number of clusters and truncated mean from the muon distributions, N_{cl}^i is the number of clusters in the combined event, and Q^i is the truncated mean for the combined event. A similar likelihood was used for pions:

$$L_\pi^i = \frac{1}{2\pi\sigma_{N_{cl}^\pi}\sigma_{Q^\pi}} e^{-\left[\frac{\left(N_{cl}^i - \bar{N_{cl}^\pi}\right)^2}{2\sigma^2_{N_{cl}^\pi}} + \frac{\left(Q^i - \bar{Q^\pi}\right)^2}{2\sigma^2_{Q^\pi}}\right]} \tag{6.6}$$

where the variables are as before, but for pions. These likelihoods were used to define the likelihood ratio, R:

$$R = \frac{L_\mu}{L_\mu + L_\pi} \tag{6.7}$$

If L_μ=1 and L_π=0, then R=1. Conversely, if L_μ=0 and L_π=1, R=0.

A cut was placed on R, such that anything above the cut was tagged as a muon, and anything below was tagged as a pion. Using the likelihood selector and the TOF data, a plot of the efficiency of muons selected as muons vs the efficiency of pions selected as muons was produced. A plot of this for a beam momentum of 140MeV/c can be seen in fig 6.14(a). Similar analysis was done for just cluster counting as well as just truncated mean, and is included in figure 6.14(a).

From the plot, when the muon efficiency is higher than 95%, only 3% of pions are mistagged as muons, while for the truncated mean, 20% of pions are mistagged and for cluster counting, 40% of pions are mistagged.

Fig 6.14(b) shows the same efficiency plot for data from window 0 at the same beam momentum and gas. From table B.4, the resolving power is 0.148, which is much lower than window 1. As expected, the cluster counting curve in the efficiency plot is much worse than in fig 6.14(a); however, there is some improvement over the truncated mean by including it. The degradation of the muon selection efficiency is likely due to the decrease in signal to noise for this run, as seen in table B.3.

A small number of the data runs were taken with the chamber at a 45° angle with respect to the beam. Many of the tracks in the SuperB drift chamber will not

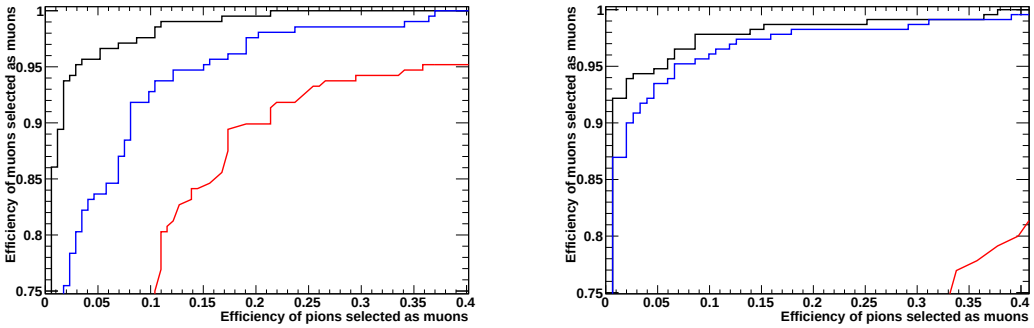

(a) Window 1

(b) Window 0

Figure 6.14: Efficiency of muons tagged as muons vs the efficiency of pions tagged as muons for cluster counting (red), truncated mean (blue), and combined (black) for 140MeV/c particles in a 90/10 gas.

be perpendicular to the beam pipe, so studying these runs is important. Fig 6.15 shows the muon tagging efficiency plot for 140MeV/c particles in one of the angled runs. The cluster counting result in this data is much better than in fig 6.14, but is still not as good as the truncated mean. Both the truncated mean and the cluster counting result do better in this run, likely since the incident particle travels through more of the gas, depositing more clusters and more charge, increasing the seperation of muons and pions. The combination of both is also better than either alone.

A similar plot of the efficiency of muons tagged as muons vs pions tagged as muons for the simulated data was produced, and can be found in fig 6.16. The behaviour of the simulation is consistent with the real data: The combination of the truncated mean and cluster counting produces efficiencies higher than either method alone.

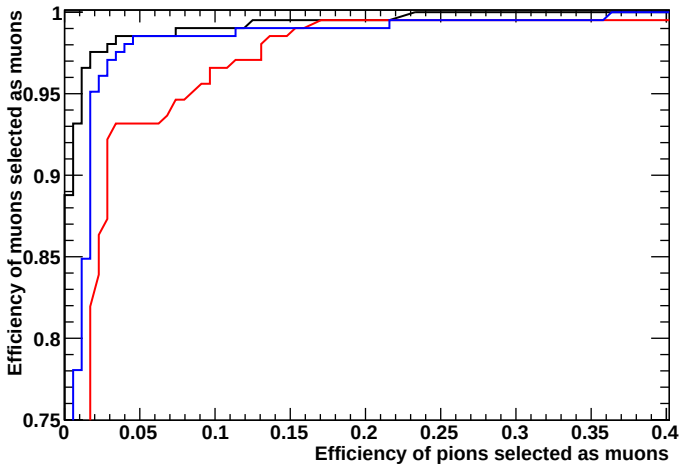

Figure 6.15: Efficiency of muons tagged as muons vs the efficiency of pions tagged as muons for cluster counting (red), truncated mean (blue), and combined (black) for 140MeV/c particles in a 90/10 gas. Data was taken with chamber at a 45° angle with respect to the beam.

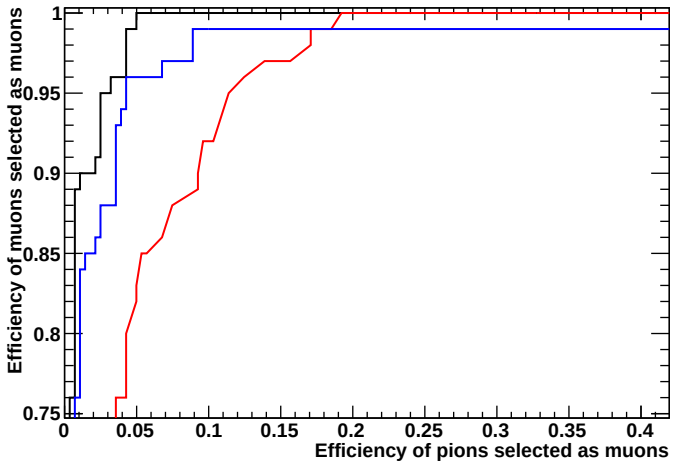

Figure 6.16: Efficiency of muons tagged as muons vs the efficiency of pions tagged as muons for cluster counting (red), truncated mean (blue), and combined (black) for simulated 140MeV/c particles in a 90/10 gas.

Chapter 7

Results

The cluster counting analysis done on the UVic chamber showed that there was a correlation between the charge deposited on the wire and the number of clusters. It was possible to compare this result with the simulation but since there was no particle ID information, it was not possible to determine how well the algorithm was working. The TRIUMF testbeam data, on the other hand, had particle ID information due to the time of flight system, making it possible to calculate the resolving power of the cluster counting. It was found that measuring the charge deposited on the wire produced a better resolving power of 1.91 compared to the resolving power of 1.57. Combining cluster counting with the measurement of charge deposited on the wire, however, did provide a significant improvement in the ability to distinguish pions and muons. In fig 6.14(a), when 1% of pions are tagged as muons, 54% of muons are correctly tagged by cluster counting alone, and 72% of muons are correctly tagged by the charge measurement alone. If both are combined, 86% of muons are correctly tagged when 1% of pions are falsely tagged. It is evident from this that significant information can be gained from cluster counting.

The results of the cluster counting presented here may have been degraded by the low signal to noise ratio of the TRIUMF data. From table B.3, it is evident that the signal to noise was barely above 20 at the best of times, and usually much worse. This could lead to degradation of the number of clusters, since the noise could be counted as clusters, or could contribute to a large averaging term in eq 6.1, reducing the difference between the noise and the clusters.

In July of 2012, there was another testbeam experiment at TRIUMF. Data was taken at a much better signal to noise than was taken previously. Different gas gains were explored as well, by changing the voltage on the anode and field wires. More data

was taken with the chamber at an angle, since many tracks in the SuperB chamber will be at an angle. With the noise under control, improvement to cluster counting is expected.

Chapter 8

Conclusion

In chapter 2, the SuperB experiment was introduced and explained. This was followed by an overview of the operation and use of drift chambers, including a description of particle identification and the potential of cluster counting in chapter 3. Chapter 4 provided an explanation as well as figures of the experiment setup for two experiments that were done to test the feasibility of cluster counting, at UVic and TRIUMF. Simulations of these experiments were done, the details of which were described in chapter 5. The analysis of the data from these experiments was demonstrated in chapter 6, including the algorithm used to count the clusters themselves, comparisons between the experiments and simulation, and comparisons between cluster counting and measurement of the charge deposited on the wire. Finally, in chapter 7, the results of the experiments were summarized, and it was stated that combining cluster counting with the charge measurement produces a significant improvement of particle identification.

Drift chambers are used to measure the tracks and identity of incident particles. The particle identity is traditionally measured using the charge deposited on a wire in the chamber by the electrons liberated by the incident particle. This method has uncertainties associated with it due to fluctuations in gas amplification as well as large charge depositions due to delta electrons. If cluster counting is used in addition to the charge deposited on the wire, it is possible to improve this measurement significantly, even in the presence of a low signal to noise ratio, as in the TRIUMF data. With better signal to noise, it may even be possible that cluster counting could produce better results.

With further study, cluster counting may prove to be useful for particle identification in a drift chamber. If so, it will be used in the drift chamber at the SuperB

flavour physics experiment in its detector system. With this and many other innovations, the SuperB experiment will be able to explore flavour and lepton physics with luminosity that is orders of magnitude larger than any other experiment has obtained to date.

Bibliography

[1] C. Hearty. Overview of the TRIUMF beam test. 2nd SuperB Collaboration meeting, Dec 2011.

[2] SuperB Collaboration, M. E. Biagini, P. Raimondi, and J. Seeman. SuperB progress reports – accelerator, 2010.

[3] SuperB Collaboration. SuperB progress reports – physics, 2010.

[4] Fabrizio Raffaelli. Private communication, May 2012.

[5] SuperB Collaboration, E. Grauges et al., F. Forti, B. N. Ratcliff, and D. Aston. SuperB progress reports – detector, 2010.

[6] G. Finocchiaro. DCH geometry options. SuperB DCH Weekly Meeting, June 2012.

[7] W. M. Yao et al. Review of particle physics. *Journal of Physics G*, 33:1+, 2006.

[8] D. H. Perkins. *Introduction to High Energy Physics*. Cambridge University Press, 2000.

[9] W. W. M. Allison and J. H. Cobb. Relativistic charged particle identification by energy loss. *Annual Review of Nuclear and Particle Science*, 30(1):253–298, 1980.

[10] R. C. Fernow. *Introduction to Experimental Particle Physics*. Cambridge University Press, 1986.

[11] A. Sharma and R. Veenhof. Properties of some gas mixtures used in tracking detectors. *CERN*, 1998.

[12] W. Blum and L. Rolandi. *Particle Detecton with Drift Chambers*. Springer-Verlag, 1994.

[13] F. Cataldi, G. Grancagnolo and S. Spagnolo. Cluster counting in helium based sasses. *Nuclear Instruments and Methods in Physics Research A*, 386:458–469, 1997.

Appendix A

Circuit Diagrams

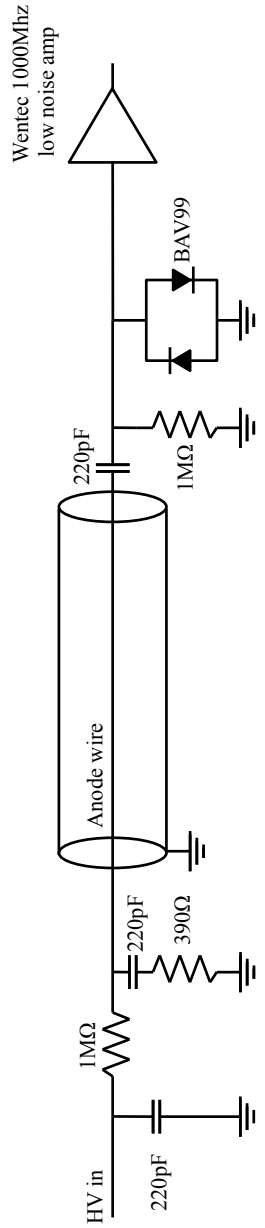

Figure A.1: Circuit diagram of UVic chamber.

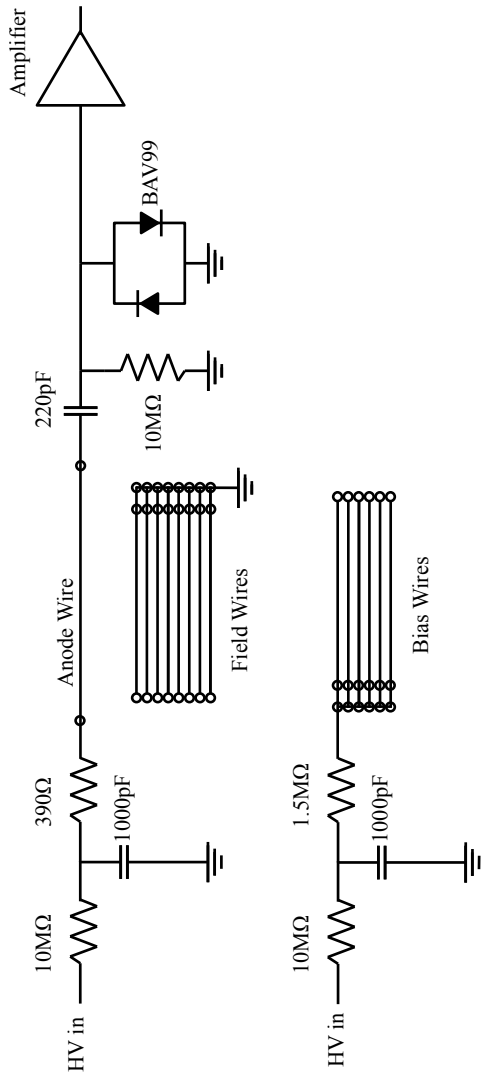

Figure A.2: Circuit diagram of TRIUMF chamber.

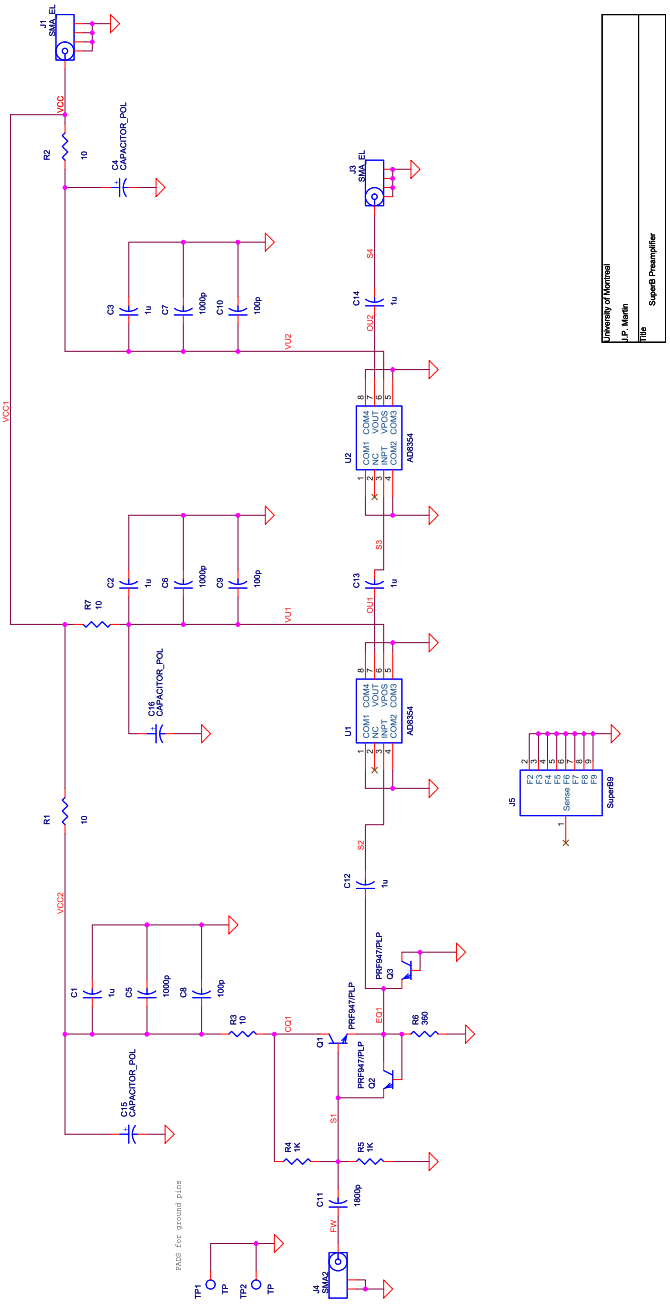

Figure A.3: Circuit diagram of TRIUMF preamp. [1]

Appendix B

Tables

Chamber	Gas	Voltage on Anode wire (V)	Voltage on Field Wire (V)	Anode Surface field (V/cm)
UVic	80% He, 20% C_4H_{10}	1950	N/A	2.82×10^5
	90% He, 10% C_4H_{10}	1650	N/A	2.38×10^5
TRIUMF	80% He, 20% C_4H_{10}	2100	1195	1.39×10^5
	90% He, 10% C_4H_{10}	1800	1023	1.19×10^5
	95% He, 5% C_4H_{10}	1580	898	1.04×10^5

Table B.1: Voltages and surface fields for UVic and TRIUMF chambers in various gases. The cathode tube/wires are grounded.

Parameter	Value	Error
A_0	322mV	15mV
t_1	370min	50min
L	3.4min^{-1}	0.3min^{-1}

Table B.2: Drift leak fits.

Momentum (MeV/c)	Window	$< PH >_{signal}$	$< RMS >_{noise}$	$< PH >_{signal}$ / $< RMS >_{noise}$
120	-2	-27.47	2.51	-10.95
	0	-40.16	2.44	-16.44
130	0	-38.54	2.87	-13.45
	0	-38.62	2.84	-13.61
140	-2	-31.14	2.54	-12.26
	-1	-33.56	2.76	-12.15
	0	-34.95	2.30	-15.2
	0*	-61.43	2.55	-24.10
	1	-57.07	2.53	-22.54
150	-2	-29.36	2.52	-11.63
	0	-37.24	2.87	-12.99
180	-2	-29.53	2.53	-11.66
	-1	-34.87	2.65	-13.17
	0	-41.05	2.58	-15.89
	0*	-57.42	2.53	-22.71
	1	-53.61	2.53	-21.22
220	-2	-25.95	2.48	-10.47
	-1	-39.13	2.52	-15.52
	0	-40.66	2.58	-15.74
	1	-51.66	2.57	-20.12

*Chamber was rotated 45° from usual position

Table B.3: Signal to noise for TRIUMF testbeam data.

Momentum (MeV/c)	Window	Threshold	n	$\Delta_{Resolving\,power}$
120	-2	-5	5	0.170
	0	-5	7	0.200
130	0	-7	5	0.164
	0	-7	4	0.401
140	-2	-6	7	0.045
	-1	-6	7	0.176
	0	-6	7	0.148
	0*	-7	5	0.400
	1	-5	7	0.248
150	-2	-6	5	0.139
	0	-6	7	0.275
180	-2	-9	5	0.109
	-1	-5	7	0.140
	0	-5	5	0.117
	0*	-7	5	0.288
	1	-5	6	0.125
220	-2	-5	5	0.259
	-1	-14	5	0.100
	0	-5	7	0.128

*Chamber was rotated 45° from usual position

Table B.4: Optimized values of threshold and number of bins averaged over, bins are 0.5ns wide.

Momentum (MeV/c)	Window	Resolving Power
120	-2	2.73
	0	2.83
130	0	0.83
	0	2.88
140	-2	0.28
	-1	1.36
	0	2.26
	0*	2.47
	1	1.91
150	-2	1.32
	0	1.78
180	-2	0.64
	-1	0.92
	0	1.17
	0*	1.54
	1	1.29
220	-2	0.25
	-1	0
	0	0.67
	1	0.13

*Chamber was rotated 45° from usual position

Table B.5: Results of truncated mean.

Particle		Cluster Counting (single wire)		Truncated Mean		Cluster Counting (40 wires)	
		Mean	RMS	Mean	RMS	Mean	RMS
Pions	Real	28	6	-1.93×10^4	0.13×10^4	1140	40
	Simulated	11	3	-1.934×10^4	0.14×10^4	440	21
Muons	Real	26	5	-1.61×10^4	0.11×10^4	1060	40
	Simulated	10	3	-1.606×10^4	0.12×10^4	403	17

Table B.6: Means and RMS values of distributions presented in figs 6.9, 6.12, and 6.13.